Effect of long-range electrostatic repulsion on pore clogging during microfiltration

Sheng Chen, Wenwei Liu, and Shuiqing Li*
Key Laboratory for Thermal Science and Power Engineering of Ministry of Education, Department of Thermal Engineering, Tsinghua University, Beijing 100084, China
(Received 12 September 2016; published 19 December 2016)

We perform computer simulations based on adhesive contact mechanics to demonstrate the clogging process of charged microparticles at the single-pore level. The effect of long-range Coulomb repulsion on clogging is characterized in terms of bulk permeability, the number of penetrating particles, and particle capture efficiency. Results indicate that the repulsion among particles delays or even totally prevents the formation of clogs. A clogging phase diagram, in the form of the driving pressure and a proposed charge parameter κ_q, is constructed to quantify the clogging-nonclogging transition. In addition, a critical state, where the capture efficiency of particles decreases to its minimum, is identified as a clogging-nonclogging criterion for repulsive particles. The distributions of the local volume fraction show that the structure of clogs is mainly determined by short-range adhesion. With relatively strong adhesion, a loose clog will be formed and it is easier for particles to penetrate. Finally, a schematic representation of the clogging process, considering both long-range repulsion and adhesion, is proposed to show the relationship between the clogging results and the interparticle interactions.

DOI: 10.1103/PhysRevE.94.063108

I. INTRODUCTION

Clogging of pores caused by microscale particles exists universally in engineering processes, including transport of biological cells [1], aerosol filtration [2], assay applications of colloidal particles [3], and microreactors [4], where both the small size of the microchannel and their consequent sensitivity to particle adhesion raise the tendency of clogging significantly [5,6]. Various clogging mechanisms have been reported. The simplest one is based on the steric effect, where particles block the pores that are smaller than their diameter [7]. Clogging also happens if the size of the pore is only a few times larger than the particles and the flow is jammed due to a sufficiently high local volume fraction of particles [8,9]. It has been suggested that common behavior exists in systems of a very different nature and scale, and the clogging process can be unified by a qualitative clogging phase diagram [10].

Adhesion due to van der Waals attraction of molecules is ubiquitous in particulate systems across almost all areas of engineering, biology, agriculture, and astrophysics [11,12]. During the microfiltration process, particles with sufficiently strong adhesion will stick onto the wall or onto other particles when they come into contact. Then bridges are formed, spanning across the channel entrance and eventually blocking the channel, even at a solid volume fraction lower than 10%, which is far less than the jamming limit [13]. Compared with van der Waals adhesion, electrostatic forces can exert their influence across a much longer distance. These long-range forces can cause profound changes in a particulate system, such as particle clustering, self-assembly [14], as well as levitation, and they provide the ability to affect and even manipulate particles at the microscales [15].

Various experimental and numerical studies have been published on the clogging phenomenon associated with adhesive or repulsive microparticles. An experimental study of aerosol filtration with long-range electrostatic repulsion is reported by [16]. The collection efficiency of a filter degrades as more particles are loaded and a minimum efficiency is obtained at steady state. Further study of Huang *et al.* observed the morphology of charged particles on a single fiber, where straight chains with branches were formed under the combined effect of adhesion and repulsion [17]. Most of the existing studies in aerosol filtration focus on either capture behavior of a single fiber or filtration performance of a macroscale filter. Few of them have dealt with the problem of the clogging-nonclogging transition at the single-pore level. With the help of microfluidic technology, there have been many observations of clogging at the single-pore level in colloidal systems in recent years. It was found that the variation of the strength of particle-particle adhesive or repulsive interactions significantly changes the clogging probability as well as the structures of the clogs [18–20]. However, among most of the experimental observations, only macroscopic properties can be measured. The inability to obtain detailed information about the various forces exerted on particles and the structure of deposited aggregates has greatly limited the understanding of these microscale clogging processes.

Particle dynamics simulation in the framework of the Lagrangian method, where interparticle forces are considered explicitly at the particle level, offers a helpful tool to understand microscale clogging. Kim *et al.* [21] analyzed numerically a two-particle behavior when the particles flow through a pore in the presence of both electrostatic repulsion and Brownian motion. The calculations demonstrated that the presence of a second particle can significantly alter the particle trajectory through long-range interactions. More recently, based on a direct calculation of the coupled equations of the motion of particles and fluid, Agbangla *et al.* investigated the dynamics of clogging at a single pore [13] as well as blockage inside straight microchannels [22] with both short-range adhesion and long-range repulsion. It was demonstrated that both the dynamics of the particle capture and the structures of clogs are drastically influenced by adhesive or repulsive interactions. In most of the simulation studies, simplified assumptions are often made that particles are "frozen" onto the wall or onto

*lishuiqing@tsinghua.edu.cn

other deposited particles when contact occurs. This is suitable only if the adhesion is significantly larger than any other forces. However, rearrangement and resuspension of deposited particles are often observed during the filtration of aerosols, where the flow stress is comparable with adhesion [23,24]. In these cases, a thorough calculation of particle motion—including normal deformation, relative sliding, rolling, and twisting—after contacts is essential to capture the structural evolution during clogging.

Recently, a Johnson-Kendall-Roberts (JKR) -based soft-sphere discrete-element method (DEM) was developed by Li and Marshall [24,25], which has also included a fast multipole method (FMM) and an average-field method to accelerate calculations of electrostatic interactions [26,27]. This novel DEM has been applied successfully to the studies of particle capture by a fiber with and without electrostatic interactions [24,28,29], where the predictions for dendrite length and capture efficiency are found to agree well with the experimental data [17].

In this paper, this DEM is extended to simulations of microfiltration to clarify the influence of long-range Coulomb repulsion on clogging at the single-pore level. A brief description of the method and the two-way coupling between the particle and the gas phase is given in the following section. Then, we try to establish the relationship between microscopic adhesive or repulsive forces and macroscopic clogging quantities, i.e., flow permeability, the number of penetrating particles, particle capture efficiency, and clogging structures. Finally, morphological changes of the deposits are shown through varying the strength of the long-range Coulomb repulsion and the short-range adhesion.

II. MODELS AND METHOD

A. Simulation conditions

A sketch of the simulated system is shown in Fig. 1. The pore is formed by two parallel cylindrical fibers with radius $r_f = 10r_p$. This system can be regarded as a basic composition unit of widely used fibrous filtration systems. The dimensions of the simulation domain are $X = 300r_p$, $Y = 30r_p$, and $Z = 40r_p$. Periodic boundary conditions are set for both fluid flow and particles along the Y and Z directions. A constant fluid velocity, U_0, in a laminar regime (Re $\ll 1$) is imposed on the inlet, and a nonslip boundary condition is applied on the fibers' surfaces. The constant rate condition can be directly compared with the applications of exhaust-gas treatment for vehicles or power plants, and it has been widely used in both experimental [2,30] and numerical studies [13,24]. Particles are randomly seeded at the inlet face with a constant volume fraction ϕ lower than 1%, and they are assumed to be neutrally buoyant to avoid the gravity effect. The ratio of the pore gap (the minimum distance between the two surfaces) to the particle radius is fixed as 10. Thus, pore clogging results only from the successive deposition of individual particles on the fibers [19,31]. Other physical parameters of our simulations are listed in Table I. Note that the surface energy γ within the range 10–15 mJ/m^2, which is the typical range of silica microspheres, is used to reflect the effect of van der Waals adhesion. The surface charge density of the particle is determined according to the typical value due to diffusion and field charging for microparticles [12].

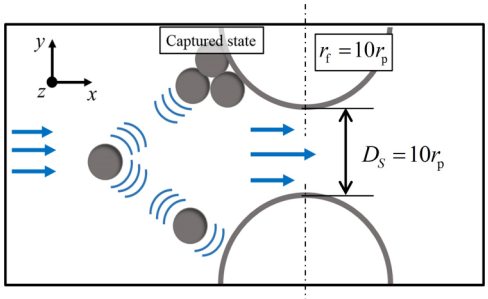

FIG. 1. Sketch of the simulated system.

TABLE I. Parameters for computer simulations.

Physical parameters	Values	Units
Particle		
Particle radius (r_p)	1.0,2.5,3.0,5.0	μm
Particle density (ρ_p)	2500	kg/m^3
Poisson's ratio (σ_p)	0.33	
Elastic modulus (E_p)	2×10^8	Pa
Restitution coefficient (e)	0.7	
Friction coefficient (τ_f)	0.3	
Surface energy (γ)	1.0–30.0	mJ/m^2
Charge density ($q/4\pi r_p^2$)	0–10.0	μC/m^2
Gas phase		
Gas density (ρ_f)	1.25	kg/m^3
Dynamic viscosity (μ_f)	1.79×10^{-5}	Pa s
Permittivity (ε_f)	8.85×10^{-12}	F/m
Inlet velocity (U_0)	0.1	m/s

B. Summary of CFD-DEM

In our simulations, the gas-phase governing equations for mass and momentum conservation are solved in the framework of the open-source MFIX code [32]. These equations are similar to those in traditional single-phase computational fluid dynamics (CFD) but with additional coupling terms due to the drag from the solid phase. The solid phase is modeled by our JKR-based soft-sphere DEM.

1. Gas phase

The governing equations of the gas phase, which is assumed to be incompressible with a constant dynamic viscosity μ_f and fluid density ρ_f, are written as

$$\frac{\partial(\phi_f \rho_f)}{\partial t} + \nabla \cdot (\phi_f \rho_f \boldsymbol{v}_f) = 0,$$
$$\frac{D}{Dt}(\phi_f \rho_f \boldsymbol{v}_f) = \nabla \cdot (-P_f \bar{\bar{I}} + \bar{\bar{\tau}}_f) - \boldsymbol{I}_{fp}. \quad (1)$$

Here, $\boldsymbol{v}_f$ and P_f are the volume-averaged gas-phase velocity and the gas-phase pressure, and $\phi_f = 1 - \phi$ is the gas-phase volume fraction. The gas-phase shear stress tensor, $\bar{\bar{\tau}}_f$, is given by

$$\bar{\bar{\tau}}_f = \mu_f[\nabla \boldsymbol{v}_f + (\nabla \boldsymbol{v}_f)^T]. \quad (2)$$

The momentum transfer term $\boldsymbol{I}_{\rm fp}$ between the gas and the solid phase on the grid node located at $\boldsymbol{x}_k$ is calculated as

$$\boldsymbol{I}_{\rm fp}^{k} = \frac{1}{V_k}\sum_{i} \boldsymbol{F}_{i,(i\in k)}^{\rm drag} K^{\rm drag}(\boldsymbol{x}_{p,i},\boldsymbol{x}_k), \tag{3}$$

where $\boldsymbol{F}_{i,(i\in k)}^{\rm drag}$ is the drag force on the ith particle located at $\boldsymbol{x}_{{\rm p},i}$ inside the kth computational cell, whose geometric volume is V_k. $K^{\rm drag}(\boldsymbol{x}_{{\rm p},i},\boldsymbol{x}_k)$ is a generic kernel with compact support that determines the influence of the particle's force on the grid node.

Given the momentum transfer term $\boldsymbol{I}_{\rm fp}$, the disturbance of particle motion on flow is well considered. The equations of the gas phase [Eq. (1)] are solved using a staggered grid finite volume scheme. The computational details of the MFIX code can be found in the user manual [33,34] as well as published papers with a series of verification tests [32]. This kind of two-way calculation method has been widely used to simulate pore clogging in flowing colloids [13], particle motion in a vortex [32], and a gas-solid fluidized bed [35].

2. Solid-phase: Discrete-element method

The DEM solves the linear and angular momentum equations of particles, where the forces and torques exerted on a particle can be written as

$$\begin{aligned} m_i\dot{\boldsymbol{v}}_i &= \boldsymbol{F}_i^{\rm tot} = \boldsymbol{F}_i^{\rm drag} + \boldsymbol{F}_i^{\rm Coul} + \boldsymbol{F}_i^{\rm con},\\ I_i\dot{\boldsymbol{\Omega}}_i &= \boldsymbol{M}_i^{\rm tot} = \boldsymbol{M}_i^{\rm drag} + \boldsymbol{M}_i^{\rm con}. \end{aligned} \tag{4}$$

In these equations, m_i and I_i are the particle mass and moment of inertia, and $\boldsymbol{v}$ and $\boldsymbol{\Omega}$ are the translational velocity and the rotation rate of a particle. The total force or torque consists of three terms: (i) hydrodynamic drag ($\boldsymbol{F}^{\rm drag}/\boldsymbol{M}^{\rm drag}$), (ii) the long-range Coulomb repulsive force ($\boldsymbol{F}^{\rm Coul}$), and (iii) forces or torques resulting from contact with other particles ($\boldsymbol{F}^{\rm con}/\boldsymbol{M}^{\rm con}$).

3. Hydrodynamic drag

Particles moving in a viscous fluid are subject to various hydrodynamic forces. The dominant force or torque in flows at small Re is the viscous drag, which can be given by the modified Stokes drag law [36]:

$$\begin{aligned} \boldsymbol{F}^{\rm drag} &= -3\pi\mu_{\rm f} d_{\rm p}(\boldsymbol{v}-\boldsymbol{v}_{\rm f}) f,\\ \boldsymbol{M}^{\rm drag} &= -\pi\mu_{\rm f} d_{\rm p}^3\left(\boldsymbol{\Omega}-\tfrac{1}{2}\boldsymbol{\omega}_{\rm f}\right), \end{aligned} \tag{5}$$

where $\boldsymbol{\omega}_{\rm f}$ is the fluid vorticity. The friction factor, $f = f({\rm Re}_{\rm p},\phi_{\rm f})$, is used to correct for particle crowding as well as particle inertia. It is given by the correlation proposed by Benyahia *et al.* [37]. This drag correlation, blending the Hill-Koch-Ladd (HKL) drag correlation with known limiting forms of the gas-solids drag function [38,39], is applicable to full ranges of Re (from 0.01 to 1000) and the gas-phase volume fraction.

4. Short-range contact forces

When particles come in contact with the fibers' surfaces or other particles, short-range contact interactions, in both normal and tangential directions, are instantly calculated with an ultrashort collision time step. In the current work, the JKR model together with a dynamic damping model are employed to describe the contact force in the normal direction. The normal force acting on particle i during a collision with particle j can be expressed by

$$F_{ij}^{\rm n} = F_{ij}^{\rm ne} + F_{ij}^{\rm nd} = -4F_{\rm C}\left(\hat{a}_{ij}^3 - \hat{a}_{ij}^{3/2}\right) - \eta_{\rm N}\boldsymbol{v}_{ij}\cdot\boldsymbol{n}_{ij}. \tag{6}$$

The first term in Eq. (6) is derived from the JKR model, which combines the effects of van der Waals adhesion and elastic deformation of particles. $F_{\rm C} = 3\pi R_{ij}\gamma$ is the critical pull-off force, and $\hat{a}_{ij}$ equals the contact radius a_{ij} normalized by its value $a_{ij,0}$ at the zero-load equilibrium state, where the elastic repulsion is balanced by the adhesive attraction. For details, see Ref. [12]. The second term of Eq. (6) represents the solid dissipation force, which is proportional to the deformation rate $\boldsymbol{v}_{ij}\cdot\boldsymbol{n}_{ij}$. The normal dissipation coefficient $\eta_{\rm N} = \alpha\sqrt{m^*k}$ is described in the literature [25], and the coefficient α is related to the restitution coefficient e by a six-order formula.

In addition to the deformation in the normal direction, the interparticle sliding, twisting, and rolling frictions are also considered and approximated by spring-dashpot-slider models [12,25]. The force and torques are expressed as

$$\begin{aligned} F_{ij}^{\rm S} &= -\min\left[k_{\rm T}\left(\int_{t_0}^{t}\mathbf{v}_{ij}(\tau)\cdot\mathbf{t}_{\rm S}d\tau\right) + \eta_{\rm T}\mathbf{v}_{ij}\cdot\mathbf{t}_{\rm S},\quad F_{ij,{\rm crit}}^{\rm S}\right],\\ M_{ij}^{\rm T} &= -\min\left[\frac{k_{\rm T}a^2}{2}\left(\int_{t_0}^{t}\Omega_{\rm T}(\tau)d\tau\right) + \frac{\eta_{\rm T}a^2}{2}\Omega_{\rm T},\quad M_{ij,{\rm crit}}^{\rm T}\right],\\ M_{ij}^{\rm R} &= -\min\left[4F_{\rm C}\hat{a}_{ij}^{3/2}\cdot\left(\int_{t_0}^{t}\mathbf{v}_{\rm L}(\tau)d\tau\right),\quad M_{ij,{\rm crit}}^{\rm R}\right], \end{aligned} \tag{7}$$

where $\boldsymbol{v}_{ij}\cdot\boldsymbol{t}_{\rm S}$, $\Omega_{\rm T}$, and $\upsilon_{\rm L}$ stand for the relative sliding, twisting, and rolling velocities between two contact particles. When these resistances reach certain critical limits, termed as $F_{ij,{\rm crit}}^{\rm S}$, $M_{ij,{\rm crit}}^{\rm T}$, and $M_{ij,{\rm crit}}^{\rm R}$, they stay constant and the particles start to slide, spin, or roll irreversibly relative to each other. These critical limits are all related to the effect of van der Waals adhesion, and they can be expressed as

$$\begin{aligned} F_{ij,{\rm crit}}^{\rm S} &= \tau_{\rm f}\left|F_{ij}^{\rm ne} + 2F_{\rm C}\right|,\\ M_{ij,{\rm crit}}^{\rm T} &= \frac{3\pi a_{ij}F_{ij,{\rm crit}}^{S}}{16},\\ M_{ij,{\rm crit}}^{\rm R} &= 4F_{\rm C}\hat{a}_{ij}^{3/2}\theta_{\rm crit}R_{ij}. \end{aligned} \tag{8}$$

The friction coefficient $\tau_{\rm f}$ is set to be 0.3, and for the critical rolling angle we use $\theta_{\rm crit} = 0.01$, based on experimental data [40]. Our adhesive DEM has been successfully applied to simulations of various adhesive particle behaviors, including particle-wall collisions [11] and deposition of particles on a fiber [28], with a series of experimental validations.

5. Long-range electrostatic repulsion

In addition to the aforementioned contact and fluid forces or torques, the presence of charged particles induces an electric field throughout the whole computation domain. The Coulomb force on a charged particle i is given by

$$\boldsymbol{F}_i^{\rm Coul} = q_i\boldsymbol{E} = q_i\sum_{j\neq i}\frac{q_j\boldsymbol{r}_{ij}}{4\pi\varepsilon_{\rm f}r_{ij}^3}, \tag{9}$$

where q_i is the charge on particle i, $\boldsymbol{r}_{ij} = \boldsymbol{x}_{{\rm p},i} - \boldsymbol{x}_{{\rm p},j}$ is the vector from the centroid of a source particle j to the

target one, and ε_f is the permittivity of the fluid. For systems with thousands of particles, direct calculation of the pairwise Coulomb interactions leads to a low simulation efficiency. Thus, a fast multiple method (FMM) is employed to reduce the computing cost from $O(N^2)$ to $O(N\log N)$, where N is the number of particles in the system, with the precision controlled by an analytic error bound [41]. In this method, all particles are grouped into boxes, and the electric field generated by a box l at the target particle $\boldsymbol{r}$ located sufficiently far away can be expressed in terms of the multipole expansion as

$$\boldsymbol{E}(\boldsymbol{r}) = \sum_{m,n,k=0}^{+\infty} \frac{(-1)^{m+n+k}}{m!n!k!} I_{l,mnk} \frac{\partial^{m+n+k} \boldsymbol{K}^{\mathrm{Coul}}(\boldsymbol{r}-\boldsymbol{r}_l)}{\partial x^m \partial y^n \partial z^k}, \quad (10)$$

where $I_{l,mnk}$ is the box moment, and the interaction kernel $\boldsymbol{K}^{\mathrm{Coul}}(\Delta r) = \Delta r/4\pi\varepsilon_f(\Delta r)^3$ depends only on the location of the box centroid $\boldsymbol{r}_l$ and the target point $\boldsymbol{r}$. For details, see Refs. [12,26].

C. Key parameters

A variety of dimensionless parameters that influence the clogging process have been proposed and discussed, including the flow Reynolds number Re, the particle Stokes number St, the particle volume fraction ϕ [13], and the ratio of pore gap to particle size, Γ [10,19]. Here, we introduce two additional parameters governing this process. The equation of motion, Eq. (4), for the ith particle in a flow can be expanded as

$$m\frac{d\boldsymbol{v}}{dt} = -3\pi\mu_f d_p(\boldsymbol{v}-\boldsymbol{v}_f) + \frac{q^2}{4\pi\varepsilon_f d_p^2}\left(\sum_{j\neq i}\frac{\boldsymbol{r}_{ij}}{r_{ij}\hat{r}_{ij}^2}\right) + 3\pi d_p\gamma\left(\sum_{i,\mathrm{cont}}\boldsymbol{n}_{ij}\left(\hat{a}_{ij}^3 - \hat{a}_{ij}^{3/2}\right)\right). \quad (11)$$

For the sake of simplicity, the friction factor in the drag force, f, is omitted. Particles are assumed to be charged with the same value q. Only the conservative force in the normal direction, F_{ij}^{ne}, is selected as a representative of contact forces. Nondimensionalizing velocity by U_0 and time by r_f/U_0, Eq. (11) becomes

$$\frac{d\tilde{\boldsymbol{v}}}{d\tilde{t}} = \frac{1}{\mathrm{St}}[(\tilde{\boldsymbol{v}}_f - \tilde{\boldsymbol{v}}) + \kappa_q\boldsymbol{\Phi}_i] + \mathrm{Ad}\Psi_i. \quad (12)$$

Here $\boldsymbol{\Phi}_i$ and $\boldsymbol{\Psi}_i$ are functions of the particles' position vectors $(\boldsymbol{r}_1,\boldsymbol{r}_2,\ldots,\boldsymbol{r}_{Np})$. Two dimensionless parameters that influence the clogging process are indicated by Eq. (12). The first is the charge parameter, κ_q, defined as

$$\kappa_q = \frac{q^2}{12\pi^2\mu_f\varepsilon_f d_p^3 U_0}. \quad (13)$$

κ_q is interpreted as the ratio of the order of magnitude of particle-particle Coulomb interaction to that of viscous drag in the flow field. It measures the ability of a particle to move relative to the local streamline due to the Coulomb force. The other parameter is the adhesion parameter, written as

$$\mathrm{Ad} = \frac{\gamma}{\rho_p U_0^2 r_p}, \quad (14)$$

which is defined as the ratio of interparticle adhesion to particle inertia [24]. This parameter estimates the sticking probability of a particle when it collides with a surface, and it has been used to quantify the effects of adhesion and particle inertia on packing structures [27,42]. For particles of size 10 μm or smaller, the Ad is usually larger than unit and the strong van der Waals adhesion leads to the formation of particle agglomerates at the pore surfaces. These agglomerates will be rearranged or broken up by the flow stress or the impact of incoming particles, which significantly disturbs the local hydrodynamic conditions [11]. A proper description of the agglomerates' behavior is thus essential to understand the underlying physics of clogging.

III. RESULTS AND DISCUSSIONS

A. Clogging-nonclogging transition

We start by studying the influence of the strength of the long-range repulsive Coulomb interaction through varying the charge parameter κ_q. During our simulation, the information from all particles (position, velocity, and forces) and flow field (velocity and pressure) was recorded simultaneously. Thus the temporal evolution of the clogging process can be easily captured.

Side views of the computational domains are shown in Fig. 2(a). Particles are projected onto the x-y plane, and the snapshots are plotted at $\tilde{t} = 120$. It can be found that a transition from the clogging state to the nonclogging one is obtained by increasing the charge parameter κ_q. Figure 2(b), taken from the case $\kappa_q = 0$ in Fig. 2(a) at a different time, clearly shows particle rearrangement during the clogging process. The red particle chains, initially aligning along the direction of the main flow, are gradually bent into short clusters. This indicates a compression of the particle cake caused by the flow stress. The dynamic behavior of particle agglomerates distinguishes our system from those with "frozen" particles and demonstrates the necessity of the DEM calculation [13].

The delay of pore clogging can be further quantified by the temporal evolution of the bulk permeability derived from the Darcy law [shown in Fig. 2(c)]. The variation of the permeability $k(\tilde{t}) = \mu_f U_0 X/\triangle P$ reflects the evolution of the pressure drop $\triangle P$ and is scaled by its initial value k_0 free of attached particles. At the initial stage of $\tilde{t} < 75$, the permeability for particles with different κ_q decreases at almost the same rate. The reason is that, during this stage, the repulsive interaction among particles is still dominated by the flow stress due to the low concentration of particles in the bulk flow and the limited number of captured particles. Once the fiber surfaces are covered by a certain number of particles, a sufficiently strong local electrostatic field is established. It forces the particle to move relative to the fluid. The subsequent permeability reduction depends significantly on the strength of the repulsive interaction. For the case with $\kappa_q = 0.14$, the scaled permeability does not drop toward 0 any longer but fluctuates around 0.4. This indicates that no clogging occurs with sufficiently strong Coulomb repulsion.

We then measure the number of particles, N^*, that flow through the pore prior to clogging. Because of the variations from one run to the next for the same physical parameters,

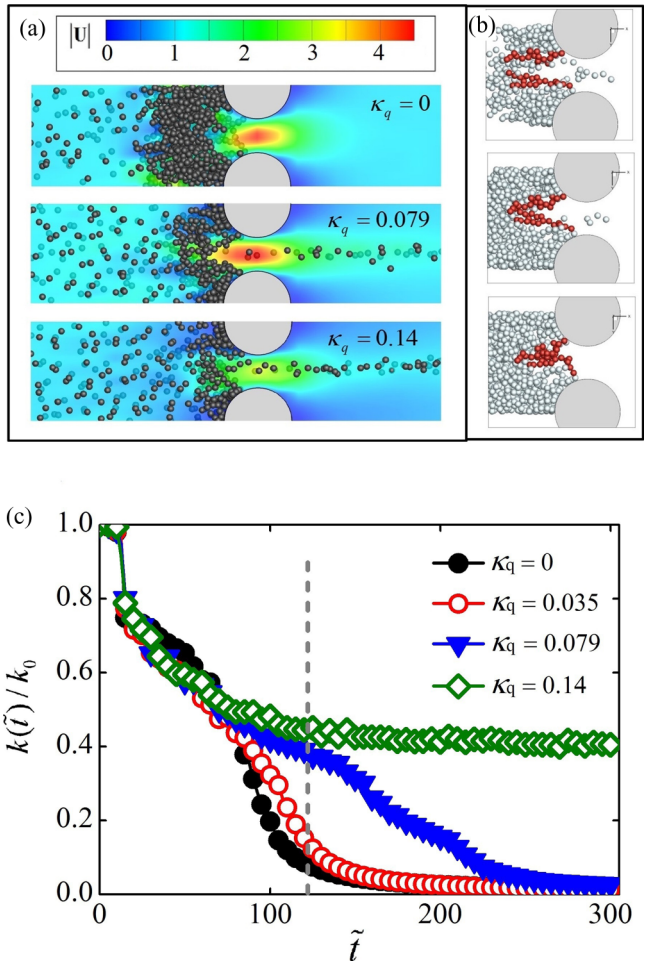

FIG. 2. (a) Side views of the particle flow projected into the x-y plane at $\tilde{t} = 120$ with Re $= 0.087$ and $\kappa_q = 0$, 0.079, and 0.14. Particles located at $z < 0$ are colored light gray, and particles at $z > 0$ are colored dark gray. (b) Schematic representation of particle rearrangement during the clogging process. (c) Scaled permeability vs time for different values of κ_q; the time is scaled by r_f/U_0.

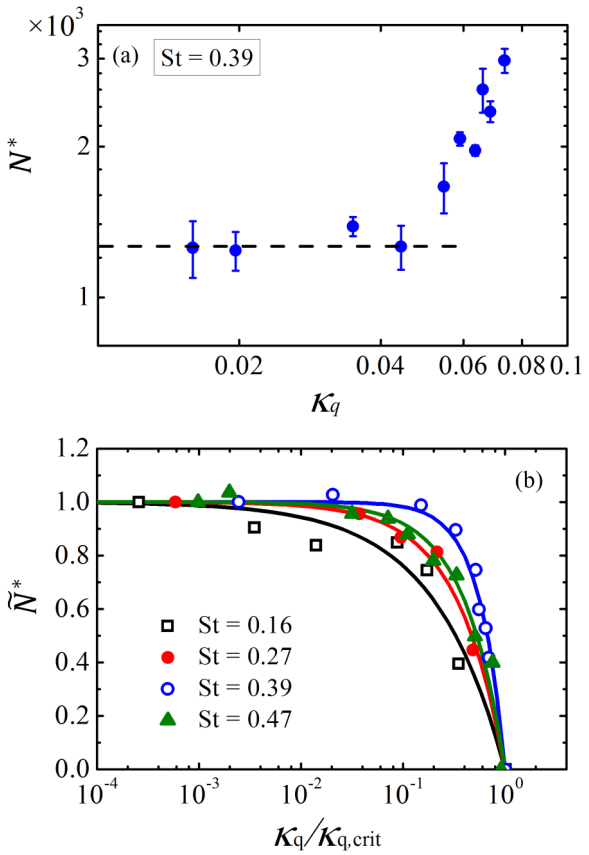

FIG. 3. (a) Number of particles, N^*, that flow through the constriction prior to the clogging as a function of Coulomb repulsion κ_q. (b) Normalized $\tilde{N}^*$ as a function of $\kappa_q/\kappa_{q,crit}$ for different St. The curves are fitted by $\tilde{N}^* = 1 - (\kappa_q/\kappa_{q,crit})^{\lambda}$ and error bars have been removed for the sake of clarity.

typically three runs with different realizations of particle injection positions were performed to provide a meaningful average and standard deviation. The change of N^* with Coulomb repulsion κ_q in a typical case is shown in Fig. 3(a), where a two-regime behavior can be found. In the first regime, at low κ_q, N^* almost remains constant. In the second regime, where N^* increases rapidly with κ_q, the particle's trajectory is modified when it approaches the deposited ones due to the strong repulsive Coulomb barrier. When κ_q increases to a certain value, no clogging occurs in all three simulation runs. Thus, this value can be regarded as the critical value $\kappa_{q,crit}$ for the clogging-nonclogging transition. No clogging can be observed with κ_q larger than $\kappa_{q,crit}$. To further characterize the transition, the number of penetrating particles is normalized as $\tilde{N}^* = N_0^*/N^*(\kappa_q)$, where N_0^* is the value for the case without Coulomb repulsion ($\kappa_q = 0$). In addition, the charge parameter κ_q is scaled by the corresponding critical value $\kappa_{q,crit}$. It can be seen from Fig. 3(b) that the normalized $\tilde{N}^*$ for particles with different Stokes numbers have a similar trend and can be fitted with power-law functions, $\tilde{N}^* = 1 - (\kappa_q/\kappa_{q,crit})^{\lambda}$, with λ and $\kappa_{q,crit}$ related to the Stokes number. The curves remain flat in the regime of very small $\kappa_q/\kappa_{q,crit}$ and then drop rapidly toward 0 when $\kappa_q/\kappa_{q,crit}$ approaches 1, indicating a fast clogging-nonclogging transition.

We have also compared our simulation results with the qualitative representation of the clogging phase diagram [10]. All the variables affecting the clogging process are grouped into three generic parameters: a length scale, such as the size ratio between the pore and the particle diameter; a compatible load parameter related to the pressure or other driving force; and an incompatible load parameter related to background noise that prevents the clogging formation. Then the transition from the clogging state to the nonclogging one can be sketched in this phase diagram.

In our simulation, the characteristic length scale is fixed by setting a constant ratio between the pore size and the particle size. Thus the three-dimensional phase diagram is reduced to a two-dimensional form, and the clogging simply arises due to the competition between the compatible load and the incompatible load. It is generally accepted that for microfiltration systems, the pressure or the driving force is responsible for the development of clogging [43]. Thus, we consider the initial pressure drop of the pore completely free of particles (P_0^*) as the compatible load. On the other hand, the pairwise repulsive Coulomb force, which prevents particles

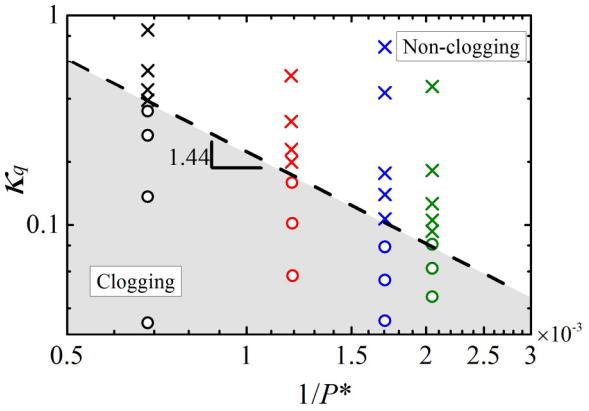

FIG. 4. Clogging phase diagram in the $\kappa_q \sim 1/P_0^*$ plane obtained for particles with long-range repulsion.

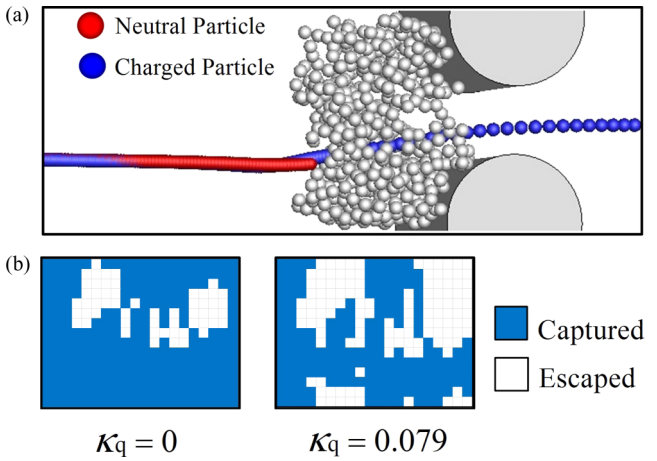

FIG. 5. (a) Two typical trajectories for natural and charged particles released at the same point. (b) Releasing points at inlet planes; white and blue parts stand for releasing points of escaped particles and captured particles, respectively.

from being captured, is supposed to be the incompatible load [31]. Then, a $\kappa_q \sim 1/P_0^*$ projection of the clogging phase diagram is obtained as shown in Fig. 4. Given a fixed $1/P_0^*$, the increase of κ_q leads to a transition from clogged systems to nonclogging ones. The dependence of the critical value $\kappa_{q,crit}$ for the clogging-nonclogging transition on $1/P_0^*$ is well described by a power law, $\kappa_{q,crit} \propto (1/P_0^*)^\beta$, with the exponent $\beta = -1.44$. This indicates that charging the particle is an effective way to reduce the possibility of clogging. The results also extend the latest proposed clogging phase diagram to the specific situation of microfiltration.

B. Measurement of particle capture efficiency

To quantify the clogging process, we introduce a method to calculate the instantaneous particle capture efficiency using simulated data. In this method, the positions of deposited particles and the flow field are output from a certain case. Then hundreds of test particles are uniformly released at the inlet plane with their trajectories followed. We set 20 releasing points in the z direction and 15 points in the y direction on the inlet plane. Consequently, the particle capture efficiency η, given by the ratio of the number of captured particles to that of total released ones, can reach a resolution as high as 0.5%. Two typical trajectories for neutral and charged particles released at the same point are shown in Fig. 5(a). The neutral particle directly hits the particle cake and is captured, while the charged particle penetrates the cake and escapes. As shown in Fig. 5(b), the remarkable growth of the area of the white part when κ_q increases from 0 to 0.079 indicates an obvious decrease in the capture efficiency.

Intuitively, the results in Sec. III A are likely caused by two mechanisms. One is that the repulsive Coulomb interaction among charged particles changes the particles' trajectory and inhibits the capture. Thus particles with a higher κ_q are more likely to penetrate the deposited particle cake. On the other hand, with distinct values of particle-particle interactions (both hydrodynamic and electrostatic ones), various types of structures are observed, which may also affect the clogging process [27]. To separate the effect of long-range repulsion from the structural effect, two series of measurements of the particle capture efficiency are performed, which are summarized in Table II. In Series 1, the effect of long-range repulsion is studied by measuring the capture efficiencies η for different κ_q based on identical structures. Since the number of deposited particles (N_{dep}) also influences the repulsion, we extract several cake structures with different N_{dep} from a basic clogging case. For instance, we fix a cake structure with $N_{dep} = 200$ and apply the long-range repulsions with $\kappa_q = 0$, 0.035, 0.079, 0.107, and 0.14 and then measure the capture efficiency with the aforementioned method, respectively. Next we repeat the measurements by fixing another cake structure with $N_{dep} = 400$, and this process is reproduced. In this way, the difference of η is independent of the structure and is only due to the effect of repulsion. In Series 2, four different structures are constructed with different Ad and κ_q. We first compare them and investigate the influences of adhesion and long-range repulsion on the structure formation. Next the four structures are fixed and η is measured respectively with the same method by removing the long-range repulsion. Such measurements can reflect the ability of particle capture of different structures.

C. A critical state as a clogging-nonclogging criterion

The effect of long-range repulsion on the dynamics of particle capture, from the measurements in Series 1, is shown

TABLE II. Parameters for capture efficiency measurement.

Cases	Structures	Repulsions
Series 1 Fig. 6(a)	$N_{dep} = 0-800$	$\kappa_q = 0$ $\kappa_q = 0.035$ $\kappa_q = 0.079$ $\kappa_q = 0.107$ $\kappa_q = 0.14$
Series 2 Fig. 9(a)	Ad = 32, $\kappa_q = 0$ Ad = 32, $\kappa_q = 0.079$ Ad = 480, $\kappa_q = 0$ Ad = 480, $\kappa_q = 0.079$	$\kappa_q = 0$

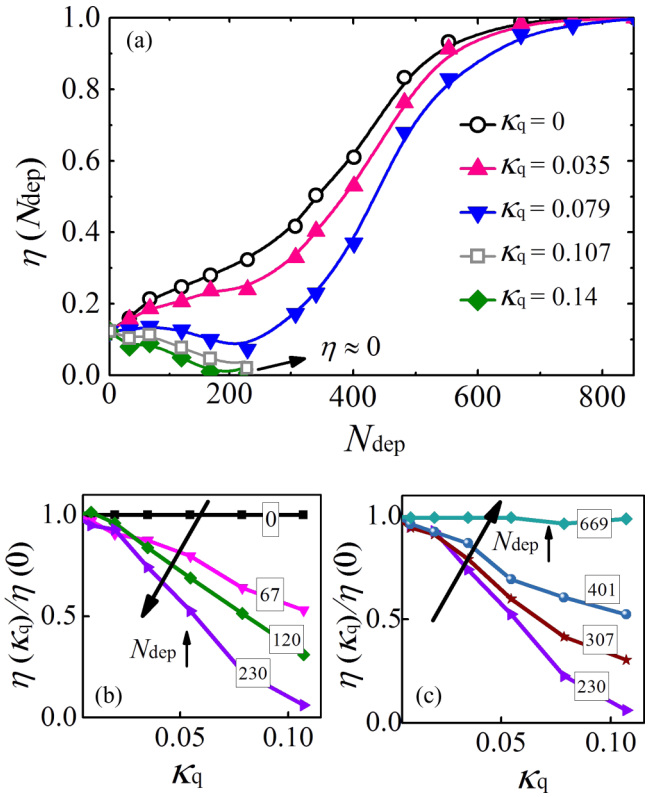

FIG. 6. (a) Particle capture efficiency as a function of the number of deposited particles. The structures for different cases are all the same. (b) and (c) The scaled capture efficiency $\eta(\kappa_q)/\eta(0)$ as a function of the charge parameter, κ_q, for different N_{dep}. Here $\eta(0)$ corresponds to the capture efficiency without repulsive interaction.

in Fig. 6(a). For particles without repulsive interaction, η increases monotonically as N_{dep} increases. This is due to the decrease of the passable channel area with the growth of the deposited layers [19]. In the presence of the repulsive interaction, η is obviously reduced and even a decreasing-increasing trend appears when κ_q reaches 0.079. When κ_q gets to the critical value $\kappa_{q,crit}$ (=0.107 in this series) or larger, the capture efficiency η decreases toward zero, leading to a nonclogging situation.

Interestingly, with either a very small or a very large N_{dep}, the effect of Coulomb repulsion is inhibited. To better illustrate this two-regime behavior, we replot the data in the form of the scaled capture efficiency $\eta(N_{dep},\kappa_q)/\eta(N_{dep},0)$ in Figs. 6(b) and 6(c), where $\eta(N_{dep},0)$ corresponds to the capture efficiency without repulsive interaction. For a given N_{dep}, this scaled efficiency is a function of the charge parameter, κ_q, and it can be simply recorded as $\eta(\kappa_q)/\eta(0)$. In the initial state, as already explained, the particles' trajectories are mainly determined by the flow stress, and the repulsive interaction among particles has only a minor effect on the particle capture efficiency. Thus relatively flat curves appear in Fig. 6(b) when N_{dep} is small. As N_{dep} increases, the fiber surfaces are gradually covered by the particles, and a sufficiently strong local electrostatic field is established to force the particle to move relative to the fluid, leading to an increase in the curves' slope.

However, when N_{dep} reaches a certain critical value (approximately 230 here), a further increase of N_{dep} will inhibit the effect of repulsion, which corresponds to the flattening of the curves in Fig. 6(c). The reason is that the steric effect on particle capture gets stronger as the passable channel area decreases. When N_{dep} reaches 700, almost all the channels are blocked and a clogging state is nearly established. These results indicate that the long-range Coulomb interaction among particles has a dramatic effect on the particle capture only when the number of deposited particles is moderate and a sufficiently strong repulsive force can push the particle through the pores inside the cake.

Summarizing the results above, we can build a better understanding of the clogging mechanisms for particles with long-range repulsion. A qualitative description of the clogging process is proposed in Fig. 7. During the initial stage of filtration, the flow stress dominates the particle capture process and the repulsion barely affects the particle trajectory [Fig. 7(a)]. As particles accumulate on the surface of the fiber, the local field of repulsion gets stronger. If the repulsion is strong enough to counteract the steric effect, a critical state, in which the capture efficiency decreases to its minimum, will be reached [Fig. 7(b)]. Then, two distinct scenarios can be identified according to the magnitude of long-range interaction. With a sufficiently strong repulsion, the deposition of particles is prevented and the capture efficiency almost drops to zero [corresponding to the case with $\kappa_q = 0.14$ in

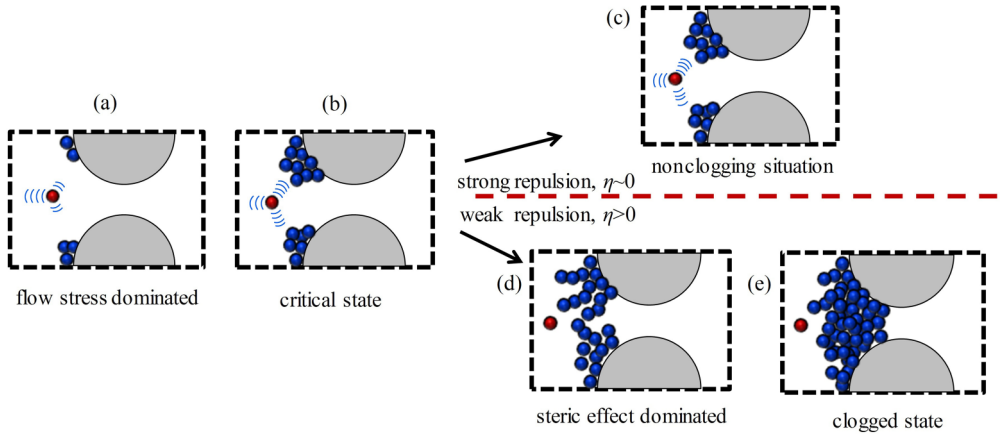

FIG. 7. Mechanism of pore clogging with particles in the presence of long-range repulsive force.

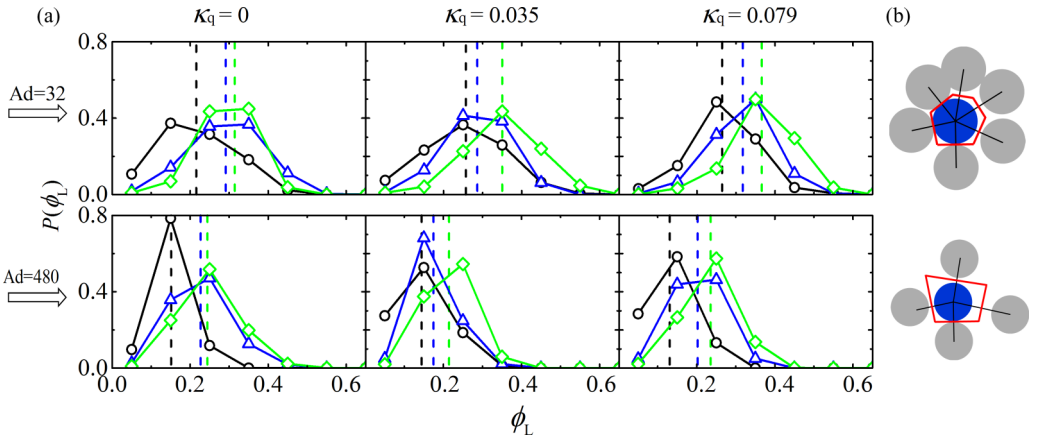

FIG. 8. (a) Distribution of the local volume fraction of clogging structures with Ad = 32 and 480 and $\kappa_q = 0$, 0.035, and 0.079. In each frame, the black scatters stand for data obtained when $N_{dep} = 500$, while the blue and green ones stand for data obtained at $N_{dep} = 1000$ and 1500, respectively, and the dashed lines indicate the average volume fractions. (b) Voronoi tessellations for a dense particle cluster and a loose one.

Fig. 6(a)]. Under these circumstances, the coming particles keep escaping through the gaps among the deposited particles, and no clogging happens [Fig. 7(c)]. On the other hand, if the repulsion is not strong enough, the minimum capture efficiency will be significantly larger than zero. Particles will continue to deposit on the fiber surface and the process enters a steric effect dominated regime, where the capture efficiency increases until the final clogged state is established [Figs. 7(d) and 7(e)]. Therefore, the minimum value of the particle capture efficiency can be regarded as a clogging-nonclogging criterion during the filtration of particles with long-range repulsion. It is worth noting that, at sufficiently small κ_q (e.g., $\kappa_q = 0$ and 0.035), the capture efficiency increases monotonically with N_{dep}. In these cases, the initial state ($N_{dep} = 0$) can be regarded as the critical state.

D. Correlation between structure and microscale forces

The spatial structures of the cake are closely related to particle-particle interactions, and they may significantly affect the clogging process. The current section characterizes the clogging structure in terms of distributions of the local volume fraction of the deposited particles. The aim is to find the correlation between structure and microscale forces, and to demonstrate the effect of structure on the clogging process.

The local volume fraction ϕ_L for each particle inside the clogging is measured. It is defined as the ratio between the particle's volume V_p to its Voronoi volume W_i, as depicted in red in Fig. 8(b). The distributions of ϕ_L, which have been grouped into sections with an increment of 0.1, are given in Fig. 8(a). For each case, the distributions are measured at three typical snapshots taken at $N_{dep} = 500$, 1000, and 1500 to illustrate structural evolution. It is easy to see the compression over time: the average volume fraction grows approximately 30% as the number of deposited particle increases. This phenomenon is mainly due to the compression exerted by the flow stress, and it is quite different from the recent results found in packing systems without a flow field, where the loose structures formed in the presence of adhesion or repulsion are stable over time [27,42].

By comparing the cases in the horizontal direction in Fig. 8(a), we find that long-range repulsion has a negligible effect on the clogging structure. It distinguishes our system from that of ballistic packings of charged particles under vacuum conditions, where long-range repulsion leads to a significantly looser structure through its influence on particle inertia [27]. The dissimilarity is mainly due to two reasons: The first is that the change of the particles' inertia, caused by long-range repulsion, is smaller in the presence of the fluid compared with that in the vacuum-packing cases. Instead of using a conventional Stokes number in fluid to reflect particle inertia, here we directly compare the variation of particle velocity for the vacuum and fluid cases. We assume a simple case, in which a charged particle with initial velocity U_0 moves across a distance L in the presence of a typical electrostatic force F_e. In the vacuum environment, the energy balance yields

$$\tfrac{1}{2}m_i U_0^2 - F_e L = \tfrac{1}{2}m_i U^2. \tag{15}$$

The variation of the velocity (inertia) of the particle scales as $\triangle U_{vacuum} \sim \frac{2F_e L}{m_i U_0}$. In the presence of fluid, this variation can be directly derived from the force balance between viscous drag and the electrostatic force F_e, yielding $\triangle U_{fluid} \sim \frac{F_e}{3\pi\mu_f d_p}$. With parameters listed in Table I, we evaluate the ratio between the inertia variations with or without fluid, and we have $\frac{\triangle U_{fluid}}{\triangle U_{vacuum}} \sim 0.2$, which confirms the statement above. On the other hand, there is a big difference between the time scales of the formation of a stable structure in these two cases. During a vacuum packing process, once the packing has been formed, the kinetic energy of the particles is immediately dissipated through inelastic deformation, relative sliding, and rolling. A mechanical stable structure, determined by the inertia-adhesion or inertia-friction competing mechanism, is formed at a time scale of particle convection $T_p = d_p/U_0$. In the present study of constant rate filtration, the pressure drop increases as the cake thickness grows and makes the cake undergo a continuous compression, which lasts through the entire clogging process.

It can be inferred that, during this process, the strength of adhesion becomes the decisive factor that affects the clogging

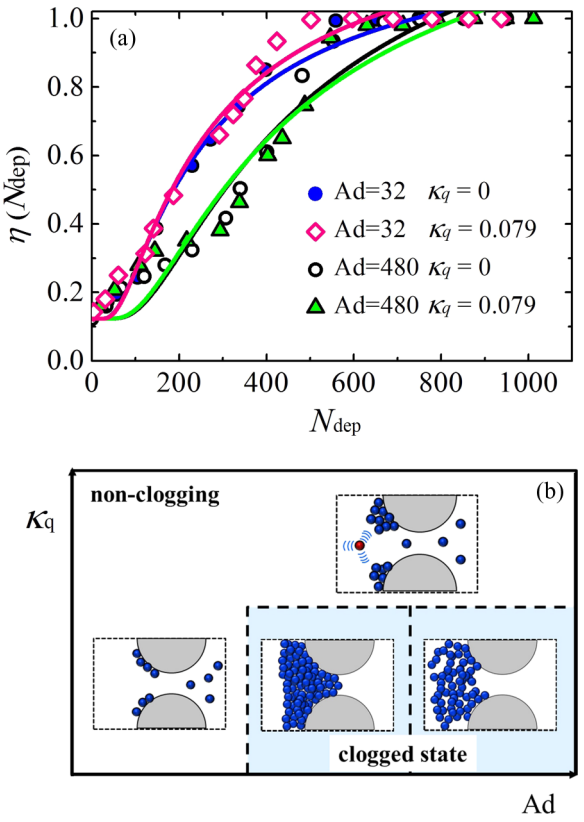

FIG. 9. (a) Particle capture efficiency η as a function of the number of deposited particles N_{dep}. The structures are taken from the cases with (blue solid circles) Ad = 32, $\kappa_q = 0$; (pink diamonds) Ad = 32, $\kappa_q = 0.079$; (black hollow circles) Ad = 480, $\kappa_q = 0$; and (green triangles) Ad = 480, $\kappa_q = 0.079$. The curves are fitted with Eq. (16). (b) Schematic representation of the clogging mechanism in the presence of both long-range repulsion (κ_q) and short-range adhesion (Ad).

structures. Thus a remarkable difference between the structure of Ad = 32 clogging and that of Ad = 480 clogging can be found by comparing the top panel to the bottom one in Fig. 8(a). This can be explained through a brief mechanical analysis of the particle agglomerate: a deposited particle will remain at rest if the contact resistances can balance the external forces or torques. Based on our contact models in Eq. (8), particles with small adhesion (Ad = 32) will be more likely to roll or slide irreversibly relative to their neighbors, which leads to a denser clogging structure [42]. For a detailed discussion of the mechanical stability of a particle cake, see [44].

E. Effect of cake structure

To investigate the effect of cake structure on particle capture dynamics, we use the method introduced in Sec. III B to measure the capture efficiency η. Four typical cake structures, which are listed as Series 2 in Table II, as well as the corresponding flow fields were extracted and measured. By removing Coulomb repulsion during the measurement, the differences between the four $\eta \sim N_{dep}$ curves reasonably reflect the influence of the cake structure, as shown in Fig. 9(a). We found that the structures formed with different Ad have a strong influence on the evolution of η, whereas the curves

TABLE III. Fitted capture efficiency as a function of N_{dep} for the four cases.

Structures	Fitting expressions
Ad = 32, $\kappa_q = 0$	$\eta = 1.17\exp(-212/N_{dep}) + 0.123$
Ad = 32, $\kappa_q = 0.079$	$\eta = 1.24\exp(-218/N_{dep}) + 0.123$
Ad = 480, $\kappa_q = 0$	$\eta = 1.50\exp(-418/N_{dep}) + 0.123$
Ad = 480, $\kappa_q = 0.079$	$\eta = 1.40\exp(-395/N_{dep}) + 0.123$

with different κ_q almost coincide with each other, which is consistent with the above discussion stating that the cake structure formation is not obviously affected by long-range repulsion. To quantitatively measure the difference, we have fitted the data in the form

$$\eta = \chi \exp\left(-\frac{N_c}{N_{dep}}\right) + \eta_0, \tag{16}$$

where χ is a prefactor and η_0 is 0.123 for all four cases, referring to the same initial capture efficiency when the fiber surfaces are free of attached particles. This expression also indicates a typical number of deposited particles, N_c, that needed to form a cake with a certain capture efficiency. The fitting expressions for the four cases are listed in Table III. It can be found that N_c for structures 1 and 2 are much smaller than the values for structures 3 and 4, indicating a faster growth of particle deposits. Since a denser clogging structure formed with small adhesion (Ad = 32) has a lower probability of particle penetration, this results in a higher capture efficiency. The results also indicate that the variation in structure caused by long-range repulsion is small and has a minor effect on particle capture. It is also interesting that, when Ad decreases further below 12, the deposited particles will be continuously resuspended into the fluid, and no stable cloggings can be formed.

Based on the above results, a schematic representation of the clogging mechanism in the presence of both long-range repulsion (κ_q) and short-range adhesion (Ad) is provided in Fig. 9(b), which summarizes different results obtained in our simulations. The presence of strong adhesion leads to the formation of dendrites and loose structures. For particles with moderate adhesion, when a deposit is formed, the particle structure is compressed by hydrodynamic forces and its permeability is relatively low. When the adhesion is sufficiently low, no stable deposits can be formed. Compared with the adhesive forces, the electrostatic repulsion exerts its influence across a much longer distance and mainly affects the capture of particles by modifying their trajectories. However, it has little effect on the structure of clogs. With sufficiently strong repulsion, the deposition of particles will be prevented once a strong local electrostatic field is established, leading to a nonclogging situation.

IV. CONCLUSIONS

We have demonstrated the feasibility of our particle dynamics simulation for the study of clogging behavior with charged microparticles. The effect of long-range Coulomb repulsion on clogging is characterized in terms of bulk permeability, the number of penetrating particles, particle capture efficiency, as well as the distributions of the local

volume fraction. It is observed that clog formation is delayed or totally prevented by repulsion, and the normalized number of penetrating particles can be well described by power-law functions. A clogging phase diagram, in the form of the driving pressure and a proposed charge parameter κ_q, is constructed to quantify the clogging-nonclogging transition. Furthermore, the instantaneous particle capture efficiency is calculated to resolve the temporal evolution of the clogging process. The results indicate that long-range Coulomb repulsion (κ_q) among particles has a significant effect on particle capture only when the number of deposited particles is moderate. In addition, a critical state, in which the capture efficiency is decreased to its minimum, is identified as a clogging-nonclogging criterion for repulsive particles. The distributions of the local volume fraction show that the structure of clogs is determined mainly by short-range adhesion (Ad). With relatively strong adhesion, a loose clog will be formed and it is easier for particles to penetrate, whereas long-range Coulomb repulsion has little effect on the structure of clogs. Finally, a schematic representation of clogging, considering the effects of both long-range repulsion (κ_q) and short-range adhesion (Ad), is proposed to show the relationship between the clogging results and the interparticle interactions.

Several avenues for future investigation have also been indicated based on our results. First, our investigation is restricted to the specific clogging problem of charged particles in the absence of an external electrostatic field. Expanding our model to include the effects of higher-order multipoles and an external field, which lead to the phenomena of particle chaining and ordering, seems worth pursuing [14,45,46]. Moreover, polydispersity and particle shape are also crucial factors that need to be considered as well, thus much more effort is warranted in the relevant studies.

ACKNOWLEDGMENTS

This work has been jointly funded by the National Key Research and Development Program of China (Grant No. 2016YFB0600602) and the National Natural Science Funds of China (No. 51390491). S.Q.L. is grateful to Jeff Marshall at Vermont and Yuliang Jin at Osaka University for fruitful discussions, and Guanqing Liu, Mengmeng Yang, Huang Zhang, and Ran Tao at Tsinghua University for their useful suggestions.

[1] H. Harrison, X. Lu, S. Patel, C. Thomas, A. Todd, M. Johnson, Y. Raval, T.-R. Tzeng, Y. Song, J. Wang *et al.*, Analyst **140**, 2869 (2015).
[2] D. Thomas, P. Penicot, P. Contal, D. Leclerc, and J. Vendel, Chem. Eng. Sci. **56**, 3549 (2001).
[3] Z. B. Sendekie and P. Bacchin, Langmuir **32**, 1478 (2016).
[4] P. Le-Clech, V. Chen, and T. A. Fane, J. Membr. Sci. **284**, 17 (2006).
[5] C. Y. Tang, T. H. Chong, and A. G. Fane, Adv. Colloid Interface Sci. **164**, 126 (2011).
[6] X. Zhu and M. Elimelech, Environ. Sci. Technol. **31**, 3654 (1997).
[7] A. Sauret, E. C. Barney, A. Perro, E. Villermaux, H. A. Stone, and E. Dressaire, Appl. Phys. Lett. **105**, 074101 (2014).
[8] K. To, P.-Y. Lai, and H. K. Pak, Phys. Rev. Lett. **86**, 71 (2001).
[9] A. Kunte, P. Doshi, and A. V. Orpe, Phys. Rev. E **90**, 020201(2014).
[10] I. Zuriguel, D. R. Parisi, R. C. Hidalgo, C. Lozano, A. Janda, P. A. Gago, J. P. Peralta, L. M. Ferrer, L. A. Pugnaloni, and E. Clément, Sci. Rep. **4**, 7324 (2014).
[11] S. Li, J. S. Marshall, G. Liu, and Q. Yao, Prog. Energy Combust. Sci. **37**, 633 (2011).
[12] J. S. Marshall and S. Li, *Adhesive Particle Flow* (Cambridge University Press, Cambridge, 2014).
[13] G. C. Agbangla, P. Bacchin, and E. Climent, Soft Matter **10**, 6303 (2014).
[14] J. S. Park and D. R. Saintillan, Phys. Rev. E **83**, 041409 (2011).
[15] P. Charbonneau and D. R. Reichman, Phys. Rev. E **75**, 050401(R) (2007).
[16] J. H. Ji, G. N. Bae, S. H. Kang, and J. Hwang, J. Aerosol Sci. **34**, 1493 (2003).
[17] B. Huang, Q. Yao, S. Q. Li, H. L. Zhao, Q. Song, and C. F. You, Powder Technol. **163**, 125 (2006).
[18] J. L. Perry and S. G. Kandlikar, Microfluid. Nanofluid. **5**, 357 (2008).
[19] H. M. Wyss, D. L. Blair, J. F. Morris, H. A. Stone, and D. A. Weitz, Phys. Rev. E **74**, 061402 (2006).
[20] P. Bacchin, A. Marty, P. Duru, M. Meireles, and P. Aimar, Adv. Colloid Interface Sci. **164**, 2 (2011).
[21] M. M. Kim and A. L. Zydney, Chem. Eng. Sci. **60**, 4073 (2005).
[22] G. C. Agbangla, Éric Climent, and P. Bacchin, Comput. Fluids **94**, 69 (2014).
[23] C. Henry and J. P. Minier, Prog. Energy Combust. Sci. **45**, 1 (2014).
[24] S. Li and J. S. Marshall, J. Aerosol Sci. **38**, 1031 (2007).
[25] J. S. Marshall, J. Comput. Phys. **228**, 1541 (2009).
[26] G. Liu, J. S. Marshall, S. Q. Li, and Q. Yao, Int. J. Numer. Methods Eng. **84**, 1589 (2010).
[27] S. Chen, S. Li, W. Liu, and H. A. Makse, Soft Matter **12**, 1836 (2016).
[28] M. Yang, S. Li, and Q. Yao, Powder Technol. **248**, 44 (2013).
[29] M. Yang, S. Li, G. Liu, and Q. Yao, AIP Conf. Proc. **1542**, 943 (2013).
[30] S. Bourrous, L. Bouilloux, F.-X. Ouf, P. Lemaitre, P. Nerisson, D. Thomas, and J. Appert-Collin, Powder Technol. **289**, 109 (2016).
[31] B. Dersoir, M. R. D. S. Vincent, M. Abkarian, and H. Tabuteau, Microfluid. Nanofluid. **19**, 953 (2015).
[32] R. Garg, J. Galvin, T. Li, and S. Pannala, Powder Technol. **220**, 122 (2012).
[33] M. Syamlal *et al.*, National Energy Technology Laboratory, Department of Energy, Technical Note No. DOE/MC31346-5824 (1998).
[34] R. Garg, J. Galvin, T. Li, and S. Pannala, https://mfix.netl.doe.gov/download/mfix/mfix_current_documentation/dem_doc_2012-1.pdf (unpublished).

[35] Z. Peng, E. Doroodchi, C. Luo, and B. Moghtaderi, AIChE J. **60**, 2000 (2014).
[36] E. Guazzelli and J. F. Morris, *A Physical Introduction to Suspension Dynamics* (Cambridge University Press, Cambridge, 2012).
[37] S. Benyahia, M. Syamlal, and T. J. O'Brien, Powder Technol. **162**, 166 (2006).
[38] R. J. Hill, D. L. Koch, and A. J. C. Ladd, J. Fluid Mech. **448**, 213 (2001).
[39] R. J. Hill, D. L. Koch, and A. J. C. Ladd, J. Fluid Mech. **448**, 243 (2001).
[40] B. Sümer and M. Sitti, J. Adhes. Sci. Technol. **22**, 481 (2008).
[41] J. K. Salmon and M. S. Warren, J. Comput. Phys. **111**, 136 (1994).
[42] W. Liu, S. Li, A. Baule, and H. A. Makse, Soft Matter **11**, 6492 (2015).
[43] M. E. Cates, J. P. Wittmer, J. P. Bouchaud, and P. Claudin, Phys. Rev. Lett. **81**, 1841 (1998).
[44] W. Liu, S. Li, and S. Chen, Powder Technol. **302**, 414 (2016).
[45] T. B. Jones, *Electromechanics of Particles* (Cambridge University Press, Cambridge, 2005).
[46] T. Shinbrot, K. LaMarche, and B. J. Glasser, Phys. Rev. Lett. **96**, 178002 (2006).